Joint design of excitation k-space trajectory and RF pulse for small-tip 3D tailored excitation in MRI

Hao Sun*, *Student member, IEEE,* Jeffrey A. Fessler, *Fellow, IEEE,*
Douglas C. Noll, *Senior member, IEEE,* and Jon-Fredrik Nielsen

I. ABSTRACT

We propose a new method for the joint design of k-space trajectory and RF pulse in 3D small-tip tailored excitation. Designing time-varying RF and gradient waveforms for a desired 3D target excitation pattern in MRI poses a non-linear, non-convex, constrained optimization problem with relatively large problem size that is difficult to solve directly. Existing joint pulse design approaches are therefore typically restricted to predefined trajectory types such as EPI or stack-of-spirals that intrinsically satisfy the gradient maximum and slew rate constraints and reduce the problem size (dimensionality) dramatically, but lead to suboptimal excitation accuracy for a given pulse duration. Here we use a 2nd-order B-spline basis that can be fitted to an arbitrary k-space trajectory, and allows the gradient constraints to be implemented efficiently. We show that this allows the joint optimization problem to be solved with quite general k-space trajectories. Starting from an arbitrary initial trajectory, we first approximate the trajectory using B-spline basis, and then optimize the corresponding coefficients. We evaluate our method in simulation using four different k-space initializations: stack-of-spirals, SPINS, KT-points, and a new method based on KT-points. In all cases, our approach leads to substantial improvement in excitation accuracy for a given pulse duration. We also validated our method for inner-volume excitation using phantom experiments. The computation is fast enough for online applications.

keywords: MRI, tailored excitation, joint design, RF pulse design, k-space trajectory design.

II. INTRODUCTION

Spatially tailored RF excitation has a range of applications in MRI, including B1 shimming [1]–[6], reduced FOV excitation [7]–[13], susceptibility artifact correction [14]–[18], and fat suppression [19], [20]. The task of designing time-varying RF and gradient waveforms for a desired target excitation pattern poses a non-linear, non-convex, constrained optimization problem with relatively large problem size that is difficult to solve directly. In conventional small-tip tailored excitation pulse design, the k-space (gradient) trajectory is pre-defined, allowing the RF waveform to be obtained using linear least-squares optimization [21]. However, for a given pulse duration, using a pre-determined k-space trajectory leads to suboptimal excitation accuracy.

Several methods have been proposed for jointly designing the k-space trajectory and RF pulse, achieving improved tailored excitation accuracy compared to pre-defined gradient approaches. These methods can be classified into two categories: sparse approximation and parametrization approaches. In the sparse approximation approach, a complete dictionary A based on the small-tip-angle approximation [22] is defined, and the joint pulse design task reduces to selecting a few k-space phase encoding locations (i.e., columns in A, typically less than 20) by either thresholded Fourier transform or sparsity-promoting or greedy algorithms. The output of those methods are discrete k-space trajectories like fast-kz/spoke pulses (discrete in kx-ky plane) [4], [23]–[26], or KT-points (discrete in 3D) [5]. Grissom et al. [27] recently combined sparse approximation with local optimization in fast-kz pulse design to improve the result and incorporate B0 inhomogeneity information. However, complex target excitation patterns require more than a few phase encoding locations, so sparse approximation approaches are used only in particular applications such as B1 shimming, and they would be difficult to use for other applications needing non-smooth target excitation patterns (especially in 3D).

In parametrization approaches to RF pulse design, the k-space trajectory is approximated by a linear combination of basis functions, and the joint pulse design task is to optimize the basis function coefficients as well as the RF waveform. Hardy expressed the k-space trajectory and RF pulse as Fourier series and then optimized the coefficients using simulated annealing [28] for 2D tailored excitation; that method is computationally too expensive for real-time tailored RF pulse design. Levin approximated the spiral trajectory by concentric rings and then optimized the radius of those rings [29]. Yip proposed a general approach for selecting basis coefficients, and applied it to optimize an EPI trajectory [30]. Shao optimized the extent of the stack-of-spirals trajectory and the fast-kz trajectory [31]. Davids optimized the extent of a 3D cross

*Hao Sun is with the Department of Electrical Engineering and Computer Science, University of Michigan, Ann Arbor, MI 48109 USA (email: sunhao@umich.edu).

Jeffrey A. Fessler is with the Department of Electrical Engineering and Computer Science, University of Michigan, Ann Arbor, MI 48109 USA.

Douglas C. Noll and Jon-Fredrik Nielsen are with the Department of Biomedical Engineering, University of Michigan, Ann Arbor, MI 48109 USA.

trajectory in $\boldsymbol{k}_x$, $\boldsymbol{k}_y$, $\boldsymbol{k}_z$ for its different shells/segments [9]. By parametrization, those methods reduced the problem dimension, and the computation complexity. However, these methods (except [9], [28]) did not explicitly consider the maximum gradient and slew rate constraint in the optimization, instead avoiding this constrained minimization problem by limiting solutions to a certain type of trajectory (e.g., EPI, spiral, stack-of-spiral). Davids et al. [9] and Hardy et al. [28] considered the constraint, but their methods require large computation time, making it impractical for online pulse design problems. Also, all the parametrization methods do not choose the trajectory type based on the information of the target excitation pattern.

In this work, we present a general approach for jointly optimizing the k-space trajectory and RF waveforms in 3D tailored excitation. Our method starts with some initial k-space trajectory (e.g., such as that obtained with one of the approaches described above), parametrizes the trajectory using 2nd-order B-spline functions, and optimizes the basis coefficients and RF waveform using constrained optimization. The peak gradient and slew rate are constrained directly during the optimization, and the trajectory is not limited to a pre-defined type such as concentric rings or EPI. We demonstrate our approach using four different k-space initializations: stack-of-spirals(SoS) [32], spiral nonselective (SPINS) [6], KT-points [5], and a new proposed initialization which we refer to as "extended KT-points" [33]. We illustrate our method in two different applications: 3D reduced FOV excitation, and spin pre-phasing. In all cases, our optimized k-space trajectories achieve improved excitation accuracy compared to the initial trajectory. Both SPINS and our proposed extended KT-points method provide good initialization.

III. THEORY

A. Problem Formulation

In joint design of a k-space trajectory and RF pulse, we want to solve the following optimization problem [30]:

$$\min_{\boldsymbol{b}\in\mathbb{C}^{N_t},\,\boldsymbol{k}_x,\boldsymbol{k}_y,\boldsymbol{k}_z\in\mathbb{R}^{N_t}} \|\boldsymbol{SA}(\boldsymbol{k}_x,\boldsymbol{k}_y,\boldsymbol{k}_z)\boldsymbol{b}\, - \boldsymbol{d}\|_{\boldsymbol{W}}^2 + R(\boldsymbol{b})$$

$$s.t. \ \|\boldsymbol{D}_1\boldsymbol{k}_x\|_\infty \le \gamma\,\Delta t\,g_{max}, \ \|\boldsymbol{D}_2\boldsymbol{k}_x\|_\infty \le \gamma\,\Delta t^2\,s_{max},$$
$$\|\boldsymbol{D}_1\boldsymbol{k}_y\|_\infty \le \gamma\,\Delta t\,g_{max}, \ \|\boldsymbol{D}_2\boldsymbol{k}_y\|_\infty \le \gamma\,\Delta t^2\,s_{max},$$
$$\|\boldsymbol{D}_1\boldsymbol{k}_z\|_\infty \le \gamma\,\Delta t\,g_{max}, \ \|\boldsymbol{D}_2\boldsymbol{k}_z\|_\infty \le \gamma\,\Delta t^2\,s_{max},$$
$$\boldsymbol{k}_x(N_t) = 0, \ \boldsymbol{k}_y(N_t) = 0, \ \boldsymbol{k}_z(N_t) = 0, \quad (1)$$

where $\boldsymbol{k}_x,\boldsymbol{k}_y,\boldsymbol{k}_z$ are N_t-length vectors containing 3D k-space trajectory locations, and $\boldsymbol{b}$ is an N_t-length vector containing the complex RF pulse values. $R(\boldsymbol{b})$ is a regularizer to limit the RF power, and we use a Tikhonov regularizer $\lambda\|\boldsymbol{b}\|_2^2$ with $\lambda = 8$ in our study. $\boldsymbol{D}_1$ and $\boldsymbol{D}_2$ are the first and second order difference matrices, $\boldsymbol{A}$ is the small-tip-angle approximation system matrix with $a_{ij} = \imath\gamma M_0 e^{\imath(k_{xj}x_i + k_{yj}y_i + k_{zj}z_i + \Delta\omega_i(t_j - T))}$, where i is the spatial index from 1 to N_s and j is the time index from 1 to N_t. T is the duration of the RF pulse. $\boldsymbol{A}$ is similar to an inverse DFT matrix, but with an additional term due to B0 inhomogeneity $\Delta\omega_i$. The RF pulse sampling interval is Δt and $\boldsymbol{d}$ is the desired

excitation pattern. $\boldsymbol{W}$ is a weighting matrix that restricts the optimization to voxels within a region of interest. The problem size varies in practice depending on the pulse length and the resolution of the target excitation pattern, but $\boldsymbol{A}$ is typically a tall matrix. $\boldsymbol{S}$ is the transmit coil sensitivity matrix; often it is simply chosen to be the identity matrix. The first and second order derivative constraints correspond to the maximum gradient (g_{max}) and gradient slew rate (s_{max}) limits of the MR scanner. The equality constraints mean the excitation k-space trajectory must end at zero, by definition [22].

B. k-space trajectory parametrization

Problem (1) is a nonlinear, nonconvex, and constrained problem that is difficult to solve. Following [30], we simplify this problem by parametrizing the k-space trajectory using basis functions:

$$\boldsymbol{k}_x(\boldsymbol{c}_x) = \boldsymbol{H}_x\boldsymbol{c}_x,$$
$$\boldsymbol{k}_y(\boldsymbol{c}_y) = \boldsymbol{H}_y\boldsymbol{c}_y,$$
$$\boldsymbol{k}_z(\boldsymbol{c}_z) = \boldsymbol{H}_z\boldsymbol{c}_z. \quad (2)$$

where $\boldsymbol{H}_x$, $\boldsymbol{H}_y$, $\boldsymbol{H}_z$ are $N_t \times L$ matrices containing L basis vectors as columns, and $\boldsymbol{c}_x$, $\boldsymbol{c}_y$, $\boldsymbol{c}_z$ are the basis coefficients. Now the joint trajectory/RF design problem (1) becomes

$$\min_{\boldsymbol{b}\in\mathbb{C}^{N_t},\,\boldsymbol{c}_x,\boldsymbol{c}_y,\boldsymbol{c}_z\in\mathbb{R}^L} \|\boldsymbol{SA}(\boldsymbol{c}_x,\boldsymbol{c}_y,\boldsymbol{c}_z)\boldsymbol{b}\, - \boldsymbol{d}\|_{\boldsymbol{W}}^2 + R(\boldsymbol{b})$$

$$s.t. \quad \|\boldsymbol{D}_1\boldsymbol{H}_x\boldsymbol{c}_x\|_\infty \le \gamma\,\Delta t\,g_{max},$$
$$\|\boldsymbol{D}_2\boldsymbol{H}_x\boldsymbol{c}_x\|_\infty \le \gamma\,\Delta t^2\,s_{max},$$
$$\|\boldsymbol{D}_1\boldsymbol{H}_y\boldsymbol{c}_y\|_\infty \le \gamma\,\Delta t\,g_{max},$$
$$\|\boldsymbol{D}_2\boldsymbol{H}_y\boldsymbol{c}_y\|_\infty \le \gamma\,\Delta t^2\,s_{max},$$
$$\|\boldsymbol{D}_1\boldsymbol{H}_z\boldsymbol{c}_z\|_\infty \le \gamma\,\Delta t\,g_{max},$$
$$\|\boldsymbol{D}_2\boldsymbol{H}_z\boldsymbol{c}_z\|_\infty \le \gamma\,\Delta t^2\,s_{max},$$
$$\boldsymbol{k}_x(N_t;\boldsymbol{c}_x) = 0, \ \boldsymbol{k}_y(N_t;\boldsymbol{c}_y) = 0,$$
$$\boldsymbol{k}_z(N_t;\boldsymbol{c}_z) = 0. \quad (3)$$

Unlike previous joint pulse design approaches that are based on predefined trajectory types (e.g., EPI or spiral) that intrinsically satisfy the gradient constraints, here we aim to solve the constrained optimization problem (3). In our approach, we do not predefine the trajectory type to form the basis, but instead use a 2nd-order B-spline basis that can closely approximate an arbitrary trajectory. In particular, for a given k-space trajectory initialization, we first approximate the trajectory using B-spline basis, and then optimize the corresponding coefficients. We choose a 2nd-order B-spline basis because the gradient constraints can be implemented efficiently, as shown next.

C. Efficient implementation of constraints

To satisfy the maximum gradient and slew rate constraints in (3), we would in general need to consider N_t time points. However, a 2nd-order B-spline basis function is a piecewise second-order polynomial (illustrated in Figure 1). Therefore, extreme points of the gradient waveform $g(t)$ (the first-order derivative of k-space trajectory) occur only at the zero-crossing point of the slew rate $s(t)$ (the second-order derivative). The slew rate $s(t)$ is a linear combination of magnitude-scaled and

shifted rect functions, and its extremes occur at all time points along the violating rect function segment, and thus it suffices to consider just one time point for each rect function. The total number of constraints that need to be considered is therefore greatly reduced by using the 2nd-order B-splines. Higher order B-splines do not have this property.

Define P_1 and P_2 as the matrices that pick the rows corresponding to the candidate extreme points of gradient and slew rate, respectively. Then we can rewrite the inequality constraints for the x gradient in the following form (only one term is shown for simplicity):

$$||P_1DH_xc_x||_\infty \leq \gamma \Delta t \, g_{max}. \quad (4)$$

Therefore, the total number of inequality constraints is reduced from $12N_t$ to $12L$ ($L \ll N_t$), where L is the number of B-splines. The number 12 arises because there are 6 constraints per time point in terms of absolute value, giving 12 when reformulating them as linear inequality constraints. For compact notation, we combine all inequality constraints as follows:

$$Uc - v \preceq 0 \quad (5)$$

where

$$U = \begin{bmatrix} P_1D_1H_x & 0 & 0 \\ -P_1D_1H_x & 0 & 0 \\ 0 & P_1D_1H_y & 0 \\ 0 & -P_1D_1H_y & 0 \\ 0 & 0 & P_1D_1H_z \\ 0 & 0 & -P_1D_1H_z \\ P_2D_2H_x & 0 & 0 \\ -P_2D_2H_x & 0 & 0 \\ 0 & P_2D_2H_y & 0 \\ 0 & -P_2D_2H_y & 0 \\ 0 & 0 & P_2D_2H_z \\ 0 & 0 & -P_2D_2H_z \end{bmatrix}, \quad (6)$$

$$c = \begin{bmatrix} c_x \\ c_y \\ c_z \end{bmatrix}, \quad (7)$$

$$v = \begin{bmatrix} \gamma\Delta t g_{max} \\ ... \\ \gamma\Delta t g_{max} \\ \gamma \Delta t^2 s_{max} \\ ... \\ \gamma \Delta t^2 s_{max} \end{bmatrix}. \quad (8)$$

The B-spine basis functions end with 0, so the k-space trajectory always ends with 0, ensuring the final three equality constraints in (3).

D. Gradient and Hessian

The optimization algorithms we investigated (see Section E) involve calculating the gradient and Hessian of the cost function (3) with respect to the coefficients (c_x, c_y, c_z). Denoting the cost function as f, one can show that the gradient is [30]:

$$\nabla_{c_x}f = 4\pi\text{Re}\{\imath H'B'A'XS'We\} \quad (9)$$

where H is the basis function, B is a diagonal matrix with the RF pulse b on the diagonal, A is the small-tip-angle system matrix, X is a diagonal matrix containing the x_i spatial coordinates, S is the diagonal coil sensitivity matrix, W is a diagonal weighting matrix, and $e = d - SAb$ denotes the excitation error. Denote the Jacobian matrix as:

$$J_x = \frac{de}{dc_x} = SXABH. \quad (10)$$

The gradient can then be written as:

$$\nabla_{c_x}f = 4\pi\text{Re}\{\imath J_x'We\}. \quad (11)$$

$\nabla_{c_y}f$ and $\nabla_{c_z}f$ have the same form except X is replaced with Y and Z, respectively.

The Hessian with respect to k_x is (see Appendix A):

$$\frac{\partial^2}{\partial k_{xi}\partial k_{xj}}f = 8\pi^2\text{Re}\{b_j^*a_j'XS'WSXa_ib_i\}, i \neq j$$

$$\frac{\partial^2}{\partial k_{xi}\partial k_{xj}}f = 8\pi^2\text{Re}\{b_j^*a_j'XS'WSXa_ib_i\}$$
$$+8\pi^2\text{Re}\{e'WSXXa_ib_i\}, i = j. \quad (12)$$

The second term in (12) is usually much smaller than the first term since e is close to zero. We therefore ignore the second term to reduce computation, and use the following approximation (with respect to c_x):

$$\nabla_{c_x}^2f \approx 8\pi^2\text{Re}\{J_x'WJ_x\}. \quad (13)$$

In addition, our problem is non-convex and the true Hessian may not be positive semidefinite, therefore $-(\nabla_{cx}^2f)^{-1}\nabla_{cx}f$ may not be a descent direction. In contrast, $J_x'WJ_x$ is always a PSD matrix and using the approximated Hessian can guarantee a descent direction.

The overall $3L \times 3L$ Hessian matrix for the x, y, z basis coefficients is then:

$$\nabla_c^2f = 8\pi^2\text{Re}\{J'WJ\}, \quad (14)$$

where $J = [J_x, J_y, J_z]$ is typically a tall matrix since the number of spatial locations N_s is much larger than the number of basis function $3L$, so the Hessian matrix $J'WJ$ can be easily stored ($3L \times 3L$), and efficiently calculated ($\mathcal{O}(N_sL^2)$).

E. Optimization algorithms

To minimize the cost function (3), we alternate between optimizing the RF waveform b and k-space trajectory coefficients c, as shown in Algorithm 1. We use conjugate gradient (CG) for the update of b, implemented using [34]. For the update of c, we want the optimization algorithm to be monotonically decreasing and feasible in each iteration. This ensures that the optimization can be terminated at any point, which is useful in practical "online" settings where patient-tailored pulses must be designed quickly. We investigated four different algorithms that are both monotone and feasible: (1) projected gradient descent algorithm with backtrack line search [35], (2) projected Levenberg-Marquardt (LM) algorithm [36], (3) interior point algorithm with backtrack line search, and (4) MATLAB 'fmincon' function using active-set solver. We implemented the algorithms and compared their
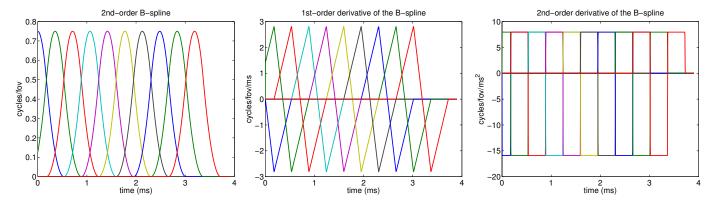
Figure 1: 2nd-order B-spline function basis, and its 1st, 2nd-order derivative. The gradient and slew rate are linear combinations of the 1st, 2nd-order derivative, respectively. The simple properties of extrema of these functions greatly reduce the number of inequality constraints that need to be considered during optimization.

speed in MATLAB on an Intel Xeon 3.3 GHz 4-core desktop with 8 GB memory.

Algorithm 1 Alternative minimization

1: Initialize: Calculate $c^{(0)}$ by B-spline curve fitting to some initial k. Obtain b using CG. Set $N_{outer} = 20$.
2: **for** i = 1 to N_{outer} **do**
3:     Approximately optimize c.
4:     Run 20 iterations CG to optimize b.
5: **end for**

In the projected LM algorithm, the projection is a quadratic programming problem that we solved using MATLAB function "quadprog". Instead of finding the exact minimizer over c, we ran the algorithms for only 2 iterations before updating b again.

The interior point algorithm used in our work is shown in Algorithm 2. In each iteration, we minimize the following cost function Φ that combines a scaled original cost function and a log barrier function, using Newton's method

$$\Phi = tf + \Psi \quad (15)$$

where t is a barrier parameter that balances the contribution of the true objective function with that of the barrier term, and $\Psi = -\sum_{i=1}^{12L} \log(u_i^T c - v_i)$. The gradient and Hessian of Ψ are:

$$\nabla\Psi(c) = \sum_{i=1}^{12L} \frac{u_i}{v_i - u_i^T c} = U^T w, \quad (16)$$

$$\nabla^2\Psi(c) = \sum_{i=1}^{12L} \frac{u_i u_i^T}{(v_i - u_i^T c)^2} = U^T \text{diag}(w^2) U, \quad (17)$$

where $w_i = 1/(v_i - u_i^T c)$. We use approximated Hessian instead of true Hessian in our implementation (line 5). α is a parameter ensuring enough decrease of the cost function, and we set it to 0.01 in our implementation (line 6). Strictly feasible condition is enforced in our implementation (line 6).

Algorithm 2 Interior point algorithm

1: Initialize: $c^{(0)}$ from the last outer iteration, $t = 20$, $N_{interior} = 2$, $N_{Newton} = 2$
2: **for** i = 1 to $N_{interior}$ **do**
3:     **for** j = 1 to N_{Newton} **do**
4:         $s = 1$
5:         Compute δ from $\text{Re}\{(J'(c^{(i)})WJ(c^{(i)})\}\delta = \nabla\Phi(c^{(i)})$
6:         **if** $\Phi(c^{(i)} + s\delta) < \Phi(c^{(i)}) - \alpha\delta'\nabla\Phi$ **AND** $c^{(i)} + s\delta$ is feasible **then**
7:             Set $c^{(i+1)} = c^{(i)} + s\delta$
8:         **else**
9:             $s = 0.5s$
10:         **end if**
11:     **end for**
12:     $t = 2t$
13: **end for**

F. Initialization

The above algorithms are local optimization algorithms that require good initialization. To demonstrate that our method can be applied to any initial k-space trajectory, we evaluated four different initial 3D trajectories: (1) stack-of-spirals (SoS) [32], (2) spiral nonselective (SPINS) [6], (3) KT-points [5], and (4) a novel trajectory design initialization approach which we will refer to as "extended KT-points" [33].

The KT-points method models the joint design problem as the following sparse approximation problem:

$$\min_{z \in \mathbb{C}^{N_t}} \|SFz - d\|_2, \text{ such that } \|z\|_0 = N_k. \quad (18)$$

F is a complete iDFT matrix and z is the RF weighting vector. This minimization problem tries to select N_k phase encoding locations from all possible k-space locations in the dictionary to best approximate d, and the non-zero term in z corresponds to the RF pulse weighting at those phase encoding locations. The B0 field inhomogeneity term in A in (1) is ignored. The reason is that the actual visiting time for each phase encoding location is undetermined when constructing the dictionary. The sparse approximation problem can be solved by either

thresholding the inverse discrete Fourier transform or using greedy algorithms. We choose a modified OMP [24] method since it can easily model the region of interest and transmit sensitivities in the system matrix. The KT-points method produces 3D k-space phase encoding locations and RF weights at those locations. Those phase encoding locations are traversed using gradient blips.

This conventional KT-point method is inefficient in 3D excitation since moving between phase encoding locations takes a large portion of the pulse duration but no RF is transmitted during this time. A natural extension is to use the k-space trajectory from KT-points but transmit continuous RF during the whole pulse duration. This is our third initialization method.

However, this simple extension may also be inefficient since the visiting order and the gradient waveform is not optimized. We therefore propose to order those phase encoding points before generating the gradient waveform. We treat this as a traveling salesman problem, and use a genetic algorithm to solve it [37]. We then generate the fastest gradient waveform to traverse those (approximately) optimally ordered points using the method in [38], [39]. This "extended KT-points" intialization is summarized in Algorithm 3. Our extension is similar to [25], but [25] does not optimize the visiting order of phase encoding locations, and was demonstrated only for 2D tailored excitation.

Algorithm 3 Extended KT-points

1: Find phase encoding locations using method [24].
2: Find the optimal visiting order using traveling salesman algorithm [37].
3: Generate the fastest gradient waveform using [38].

IV. METHODS

A. Simulation study

We applied our method to two pulse design problems: 3D inner-volume excitation and spin prephasing. For inner-volume excitation, we excited a $6 \times 6 \times 6$ cm^3 cube with 10 degree flip angle using an RF pulse of approximate duration 4 ms transmitted on a single transmit coil. We simulated the excitation results for a $64 \times 64 \times 8$ matrix over a $24 \times 24 \times 16$ cm^3 FOV. To reduce computation time, we downsampled the matrix to $32 \times 32 \times 8$ for optimization. We used a measured B0 field map from an Agar ball phantom in the simulation. We measured the B0 field map by acquiring spoiled gradient-echo (SPGR) images with two different echo times (3 ms and 5.3 ms), and taking the phase difference on a voxel-by-voxel basis. We assume uniform coil transmit sensitivity.

For spin prephasing [14], we want to achieve the following excitation pattern: $\boldsymbol{d}(\Delta\boldsymbol{\omega}(\boldsymbol{r})) = e^{i\Delta\boldsymbol{\omega}(\boldsymbol{r})T_{\text{free}}} \sin \alpha$, where α is the flip angle (uniform for all spins), $\Delta\boldsymbol{\omega}(\boldsymbol{r})$ is the B0 field map, and T_{free} is the free precession time. The goal is to achieve refocusing T_{free} after the excitation[1]. Prephasing

---

[1] We use the convention $\omega = \gamma B$ in our paper. Since the free precession is rotated clockwise with a positive B field, the accumulated phase is in the negative direction: $\theta_f = -\omega T_{\text{free}}$

pulses may be used to compensate for susceptibility (T2*) signal loss, and are needed in the "small-tip fast recovery" steady-state imaging sequence being developed by our group [14]–[16]. We designed a prephasing pulse with 10 degree flip angle, 2.5 ms T_{free}, and measured B0 field map from a human brain. We simulate with $64 \times 64 \times 8$ matrix size and $24 \times 24 \times 4$ cm^3 FOV.

We evaluated four different algorithms for parametric optimization, and four initializations, but we did not compare all 16 combinations. Instead, we first compare the speed of optimization algorithms for inner-volume excitation using the extended KT-point initialization. After finding the fastest algorithm, we compared the excitation accuracy using different initializations, both before and after constrained optimization.

Figure 2 shows the four different k-space trajectory initializations used in the inner-volume excitation. The prephasing problem uses the same SoS and SPINS initialization, but different KT-points and extended KT-points initialization since they are excitation pattern dependent. The parameters for SoS and SPINS trajectories were manually tuned to achieve good initial excitation results. For SoS, we used 5 spiral stacks with 17 cm excitation FOV in z direction, and each spiral has 6 cycles with 24 cm excitation FOV in the x-y plane. For SPINS, we set the maximum extent of k-space to 0.48 cycles/cm, polar angular velocity to 3π/ms, azimuthal angular velocity to 2π/ms, and speed and position of transition between slow and radial phase to 10 and 0.5 [6]. The resulting SPINS trajectory is accelerated using the fastest gradient waveform [39]. There are small variations in the pulse length since it can not be directly constrained when generating different initializations. For fair comparison, we tuned the parameters to generate initial trajectories around 4 ms, and then cut all of them to the same length as the shortest one, resulting in approximately 3.8 ms and 3.9 ms pulse length for all initial trajectories for inner-volume excitation and prephasing problem, respectively (corresponding to 954 and 982 time points sampled at 4 μs).

In all simulations, we created a region of interest (ROI) that covers the whole object by thresholding the non-selective SPGR images used in B0 field map acquisition, resulting in a total number of 2243 spatial positions on the 32x32x8 grid for inner-volume excitation. Therefore, the system matrix $\boldsymbol{A}$ is a 2243 by 954 matrix in the inner-volume excitation case and it is constructed explicitly. The prephasing problem has similar problem size. When the problem size gets much larger, we may have to implement the system matrix implicitly using NUFFT [40].

B. Phantom experiment study

We evaluated our method for an inner-volume excitation task on an Agar ball phantom using a GE MR750 3.0T clinical scanner. We used the same target pattern as our inner-volume excitation simulation (i.e., a $6 \times 6 \times 6$ cm^3 cube). We measured the B0 field map by acquiring spoiled gradient-echo (SPGR) images with two different echo times (3 ms and 5.3 ms), and taking the phase difference on a voxel-by-voxel basis. This B0 field map was used in the simulation study (Figure 5). We designed the RF pulse using the same parameter settings as we
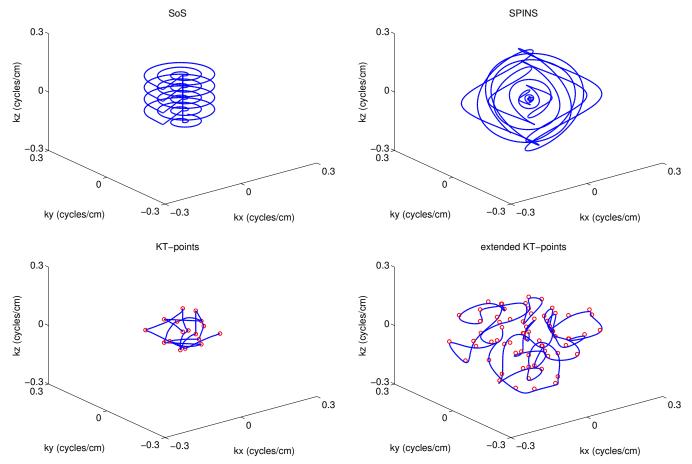
Figure 2: Different k-space trajectory initializations for the inner-volume excitation: stack-of-spirals (SoS); SPINS; KT-points; and "extended KT-points". For KT-points and extended KT-points initializations, the discrete KT-points are included in the plot as red circles. Note that the extended KT-points trajectory does not pass through the discrete KT-points exactly, due to the small gradient/slew rate violation in the fastest gradient waveform algorithm [38], [39], as also reported in [41]. KT-points and extended KT-points selectively traverse the k-space based on the target excitation pattern. The extended KT-points method manages to traverse a larger k-space region than the simple KT-points initialization because of the improved visiting order and the use of a time-optimal gradient waveform.

did in the simulation. For readout, we used an SPGR sequence with 500 ms TR and minimum available TE.
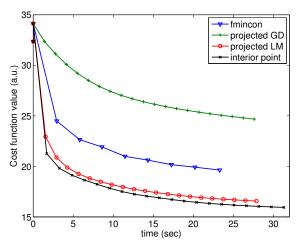
V. RESULTS

A. Simulation results

Figure 3 shows the cost function value and normalized root mean square error (NRMSE) of the excitation versus computation time for different algorithms in solving the parametrized constrained optimization (3) in the inner-volume excitation case using extended KT-points as the initialization. NRMSE is defined as $\frac{\|SAb - d\|_2}{\sqrt{N_s} \sin \alpha}$, where α is the target excitation angle, and the transmit sensitivity matrix S is set to identity matrix. The interior point and projected LM algorithms are much faster than the simple projected GD and MATLAB 'fmincon'. Compared to projected LM, the interior point algorithm is slightly faster and its final k-space trajectory has lower slew rate (not shown). We use the 'active-set' solver

for the MATLAB 'fmincon' function. There is an 'interior-point' solver for the MATLAB 'fmincon' function, but it is not strictly feasible in each iteration and its speed is slower than our projected LM and interior point implementations. The shapes are similar between the NRMSE plot and the cost function value plot. There is a small increase in the first iteration for projected GD. This is because the first point in the plot corresponds to the initial k-space trajectory, not the initial approximation using B-spline basis, and applying the approximation can lead to a potentially higher cost and/or NRMSE in the first iteration. Based on these results we chose the interior point algorithm for all subsequent simulations.

Figure 4 shows the k-space trajectory before (dashed line) and after (solid line) the interior point optimization using an extended KT-point initialization for prephasing excitation. The gradient waveform, slew rate, and RF pulse are also shown in the figure. The peak gradients are well below the 4 G/cm limit we set, while the slew rates are close to the imposed limit of 15 G/cm/ms. The differences between the final k-
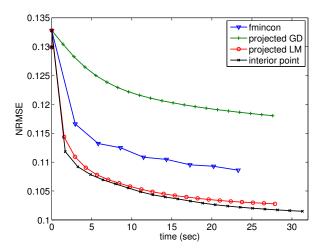
Figure 3: Convergence speed of different algorithms used to solve the parametrized constrained optimization problem (3): (Left) Cost function value versus time. (Right) NRMSE versus time. There are two data points at time 0: the lower one is using the initial k-space trajectory and the higher one is using the k-space trajectory after B-spline fitting. The fitting at the beginning of optimization slightly increases the NRMSE and the cost function value. The interior point and projected LM algorithms converge much faster than the other two, with the interior point algorithm slightly faster.

space trajectory and the initialization are also included in the figure.

Figure 5 shows inner-volume excitation results. Four different methods are used as initialization to the parametrized optimization (3). Bloch simulation results before and after initialization are shown in the left and right column, respectively. Without parametrized optimization, our extended KT-points method generates the least excitation error with the shortest pulse. With parametrized optimization, all methods are improved by 10~30%. Using SPINS or extend KT-points as initialization generate the best final results. The peak RF is below the limit of our GE scanner (0.25 Gauss). The measured 10 sec average SAR (or the integrated RF power) is below 0.3 W/Kg, much lower than the 6.4 W/Kg limit for human brain.

Figure 6 shows the excitation error of the prephasing problem using the same 8 methods. Similar to the reduced FOV excitation case, optimization greatly reduced the excitation error for all initializations. Without interior point optimization, SPINS generated the best result. Extended KT-points generated a good result, but not as good as in the reduced FOV case, probably because the energy in k-space is more uniformly distributed, so the sparsity-based extended KT-points method is not as effective as it is in the reduced FOV case.

B. Phantom experiment results

Figure 7 shows a phantom experimental result for inner-volume excitation. The experiment demonstrated that our pulse is feasible in practice, and the results agree with our conclusion that the optimization improves excitation accuracy for a given initialization. The NRMSEs of the magnitude excitation patterns are reported for each method (excitation phases are excluded in the NRMSE calculations because the transmit and receive coil phase were not measured).

VI. DISCUSSION

We have shown that the proposed optimization improves excitation accuracy for all initial k-space trajectories tested. The improvement in excitation relative to that produced by the initial pulse depends on both the initial k-space trajectory and the target excitation pattern. For example, for target patterns with concentrated energy in excitation k-space, an initialization based on sparse approximation may already be close to optimal. In other cases, the optimization step may significantly improve the excitation compared to the initialization. However the simulation and experimental evidence presented here suggests that the proposed optimization can be used to improve excitation accuracy for any initialization that is (at least locally) suboptimal.

For the examples shown here, the computation time for the parametric optimization step is typically less than 1 minute. Using KT-points or extended KT-points requires additional optimization to form the initial pulse, which takes less than 1 minute. The overall computation time for all methods tested in this study is less than 2.5 minutes, fast enough for normal online pulse design, particularly with a faster computer.

We conclude that both SPINS and extended KT-points provide good initializations. The extended KT-points initialization performs extremely well in the inner-volume excitation case, probably because the inner-volume excitation pattern has a sparser corresponding k-space weighting than the prephasing target pattern. SPINS initialization has shorter computation time (no sparse approximation step). However, it has the disadvantage that more parameters (e.g., k-space extent, rotation speeds) need to be manually tuned in the design [6], while the extended KT-points method generates a trajectory automatically without manual parameter tuning.

We used 2nd-order B-spline functions to represent the k-space trajectory. B-splines are widely used to represent general smooth curves because the low-order polynomials are fast to
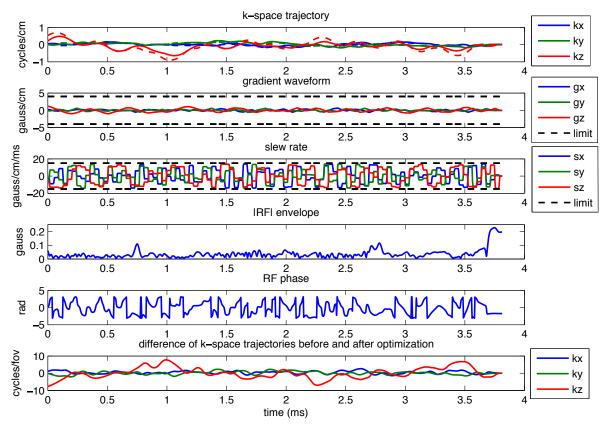
Figure 4: Example k-space trajectory, gradient waveform, slew rate and RF waveform for spin prephasing simulation. The extended KT-points k-space trajectory before (dashed line) and after 20 iterations of alternating optimization with interior point algorithm (solid line) have similar shape. Their difference is plotted in the bottom row of the figure with unit cycles/fov. Both gradient and slew rate are within our constraint, but the slew rates are closer to the limit.

evaluate and it has a finite support. Also, 2nd-order B-splines provide the additional benefit that the number of constraints can be reduced as shown before. In our study, we used the same basis functions for k_x, k_y and k_z. We used 100 basis functions to represent one component of a k-space trajectory (i.e., 100 for k_x, 100 for k_y, and 100 for k_z) of length around 3.8 ms (corresponding to 954 time points for one component), and we found that the resulting fits are quite good for all four k-space initializations. We also simulated using different number of basis functions (L = 20 to 200), and observed that the final NRMSEs are quite similar for L = 50 to 200 (not shown). The computational time increased from 20 sec (L = 20) to 50 sec (L = 200). We obtained good results using this basis, but we do not claim this is the optimal choice.

In Figure 4, we note that neither the gradients nor the slew rates reach their limits in some portion of the excitation pulse, indicating that the overall pulse could be shortened without sacrificing excitation accuracy, but at the cost of increased RF power. We also found that the slew rates are usually closer to their limits than the gradient amplitudes based on our experience, indicating that the gradient constraints could potentially be eliminated to accelerate the algorithm in most cases.

Our choice of the iteration number and regularization parameter are relatively heuristic. We choose the iteration number such that the total computation time (including ex-

tended KT-point initialization) is limited to 3 minutes for the different excitation tasks we have tested. Increasing the iteration number usually further improves the excitation result, but the improvements are usually very small based on our experience. A smaller RF regularization parameter leads to smaller excitation error calculated using the small-tip approximation model, but it has to be large enough such that the resulting RF pulse satisfies peak RF and SAR constraints, and the small-tip approximation. We choose a number that satisfies those requirements in most cases based on our experience. A better approach may be adding RF inequality constraints instead of a regularization term in the cost function.

Parallel transmission is a means of improving the tailored excitation accuracy using multiple coils [42]–[44]. We demonstrated our proposed method only for single coil excitation in this paper, but it could be easily extended to parallel excitation. The problem formulation in the parallel transmit case can follow the equations in Yip's joint pulse design paper [30]. In particular, we simply modify the cost function (1) to include the coil sensitivities of all coils. For the optimization algorithms, we can use the spatial domain method for parallel transmit RF pulse design [44] to update the RF waveform, and use the interior point method in our paper to update k-space trajectory but with a modified gradient and Hessian (see section 7.5 of [45] for more detail).

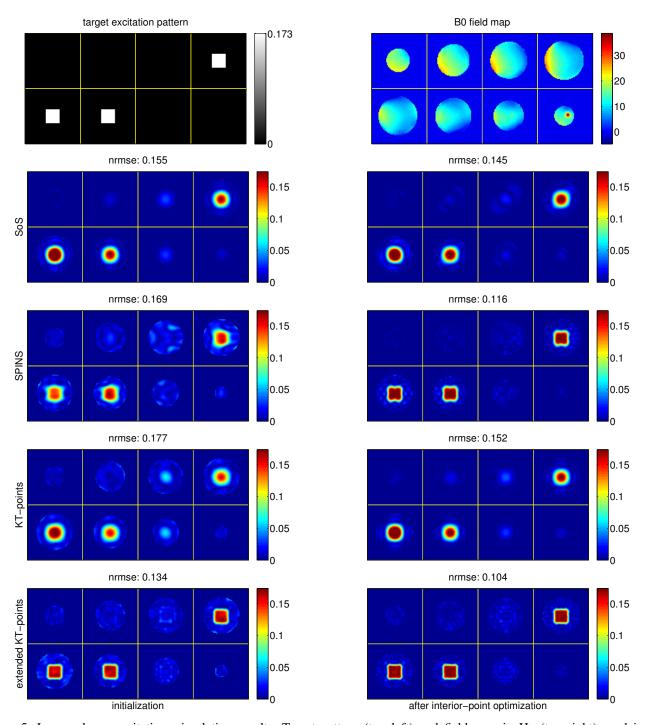Sometimes, constraints on total gradient and slew rate across

Figure 5: Inner-volume excitation, simulation results. Target pattern (top left) and field map in Hz (top right) used in the simulation. Row 2 to 5: results for different pulse design methods: left column contains the results of initialization pulse, right column contains the results after optimization using interior point algorithm. Four initialization methods were investigated: from top to bottom: SoS, SPINS, KT-points, our extended KT-points. All pulses have 3.8 ms pulse length. Optimization always improves the excitation results, reducing the NRMSE by 10 to 30% depending on the initialization method. Using extended KT-points as the initialization gave the best results.
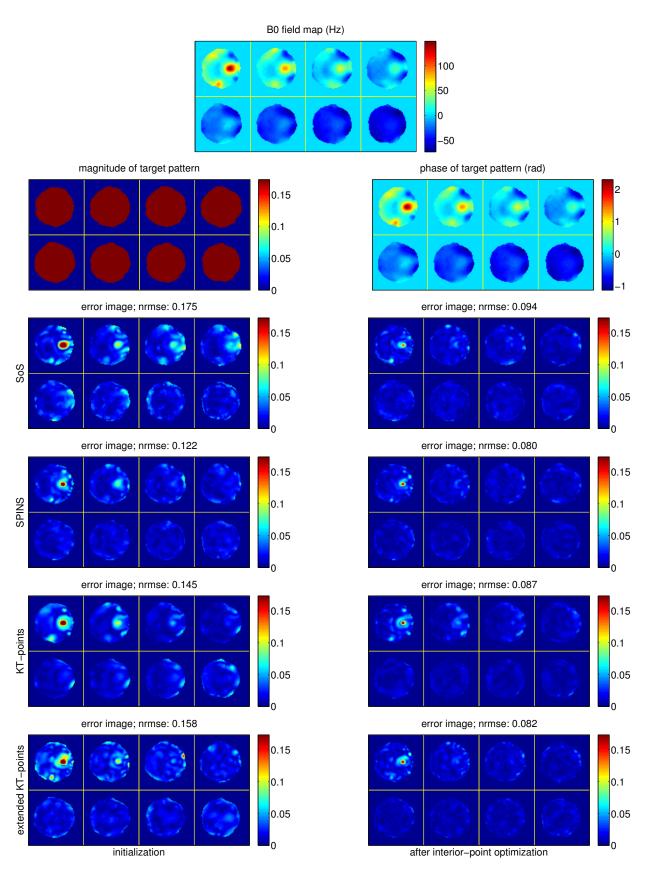
Figure 6: Prephasing excitation, simulated excitation error (magnitude of the complex-value difference between target pattern and Bloch simulated pattern). The B0 field map is acquired from a human brain scan, shown in Hz. The target excitation pattern has uniform 10 degree flip angle and B0 dependent phase ($\Delta\omega_i T_{\text{free}}$). The excitation error images for different initializations are ordered in the same way as Figure 5, and the pulse lengths are 3.9 ms for all. We want small error (dark blue) in the whole image. Without optimization, SPINS performs the best in this case. Interior point optimization substantially reduces the excitation error for all initializations, and SPINS and extended KT-points produce final results with similar accuracy in this prephasing case.
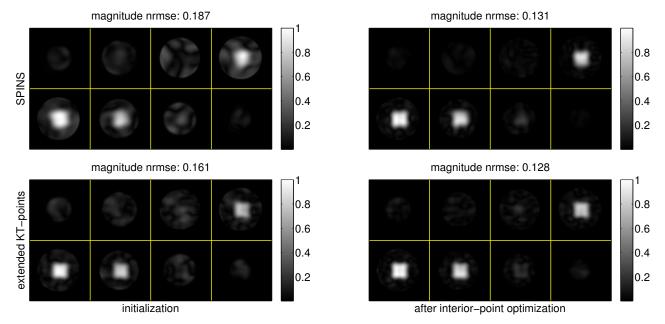
Figure 7: Inner-volume excitation, phantom experimental result. The target excitation pattern and B0 field map are the same as shown in Figure 5. Two initialization methods were tested in the experiment: SPINS (top row) and extended KT-points (bottom row). The left column contains the acquired image using the initialization excitation pulse, and the right column contains the image using the optimized excitation pulse. The magnitude NMRSEs are labeled above the corresponding images. The experimental result agrees well with simulation: the extended KT-points initialization produces a relatively good result, and the optimized pulses improve the excitation results for both initializations.

channels are also enforced. Our method can be extended to this case by modifying (6) and (8) since the constraints on total gradient and slew rate can be written as linear inequality constraints as well.

For the inner-volume excitation, the maximum outer-volume flip angle may be also important. With a 10° inner-volume flip angle, the maximum outer-volume flip angles (before/after optimization) in our simulation study were $3.5^o/3.4^o$ (SoS), $3.7^o/2.6^o$ (SPINS), $2.5^o/2.7^o$ (KT-points), $2.8^o/2.2^o$(extended KT-points) excluding the boundary voxels (most of the excitation error occurred at the boundary between inner volume and outer volume, but those boundary voxels are usually not important in practice since we can slightly increase the readout FOV to cover those boundary voxels, so the outer-volume mask was eroded by five pixels in the calculation). Our optimization reduces the maximum outer-volume excitation for all initializations except KT-points. This is not surprising since the maximum outer-volume excitation is not the direct minimization target in our simulation. In practice, a higher weighting could be applied to the outer volume to further reduce the outer-volume excitation, or a minimax pulse design method could be used [26], [45].

In addition to the phantom experimental data we have shown in this paper, we have previously evaluated our extended-KT points initialization (which has very high slew rate) in phantom and *in vivo* experiments in [13], [33]. We used the initialization instead of the fully optimized k-space trajectory and RF waveform in that study because we had not fully developed the constrained optimization part of our method at that point. We also measured the output k-space trajectory

of the extended KT-point initialization and it agrees well with the nominal k-space trajectory (see [33]), indicating that eddy currents may not be a problem for our implementation on our GE MR750 3.0T human scanner. We believe all those experimental studies demonstrate the feasibility of the proposed method. If a scanner has higher gradient distortion, a gradient system characterization and k-space trajectory estimation method like [46] may be used to pre-compensate the designed gradient waveforms.

In the phantom simulation and experiment, we have a relatively small B0 inhomogeneity. To evaluate a case with high B0 inhomogeneity, we also simulated an inner-volume excitation with acquired brain B0 field map and cylinder target excitation pattern. The results are included in the supplementary material, and again demonstrate that our optimization can significantly reduce the excitation error.

VII. Conclusions

We have proposed a new joint design method for 3D tailored excitation that can improve excitation accuracy for arbitrary k-space trajectory initializations. We also proposed a new k-space initialization method, extended KT-points, that appears to be better or at least as good as several existing 3D trajectory choices. The total computation time is short enough for online applications. We anticipate that the proposed 3D selective excitation pulses will find use in inner-volume imaging and related applications.

VIII. Appendix

We derive the Hessian of the cost function (1) with respect to $\boldsymbol{k}$ here. Define the excitation error term $\boldsymbol{e} = \boldsymbol{d} - \boldsymbol{S}\boldsymbol{A}(\boldsymbol{k}_x, \boldsymbol{k}_y, \boldsymbol{k}_z)\boldsymbol{b}$ and the $N_t \times 1$ temporal vector:

$$\boldsymbol{p}_x = \nabla_{\boldsymbol{k}_x} f = \nabla_{\boldsymbol{k}_x} ||\boldsymbol{e}||_{\boldsymbol{W}}^2, \qquad (19)$$

then the jth element of $\boldsymbol{p}_x$ is

$$p_{xj} = 2\mathrm{Re}\left\{\boldsymbol{e}'\boldsymbol{W}\boldsymbol{q}_{xj}\right\} \qquad (20)$$

where

$$\begin{aligned}\boldsymbol{q}_{xj} &= \frac{\partial \boldsymbol{e}}{\partial k_{xj}} \\ &= -\imath 2\pi \boldsymbol{S}\boldsymbol{X}\boldsymbol{a}_j b_j \qquad (21)\end{aligned}$$

Then, the (i,j)th elements of the Hessian matrix are:

$$\begin{aligned}\frac{\partial^2 f}{\partial k_{xi} k_{xj}} &= \frac{\partial \boldsymbol{p}_{xj}}{\partial \boldsymbol{k}_{xi}} \\ &= 2\mathrm{Re}\left\{\frac{\partial \boldsymbol{e}'}{\partial k_{xi}}\boldsymbol{W}\boldsymbol{q}_{xj} + \boldsymbol{e}'\boldsymbol{W}\frac{\partial \boldsymbol{q}_{xj}}{\partial k_{xi}}\right\} \\ &= 2\mathrm{Re}\left\{\boldsymbol{q}_{xi}'\boldsymbol{W}\boldsymbol{q}_{xj} + \boldsymbol{e}'\boldsymbol{W}\frac{\partial \boldsymbol{q}_{xj}}{\partial k_{xi}}\right\} \qquad (22)\end{aligned}$$

For the second term, when $i \neq j$,

$$\frac{\partial \boldsymbol{q}_{xj}}{\partial k_{xi}} = 0. \qquad (23)$$

When $i = j$,

$$\frac{\partial \boldsymbol{q}_{xj}}{\partial k_{xi}} = 4\pi^2 \boldsymbol{S}\boldsymbol{X}\boldsymbol{X}\boldsymbol{a}_j b_j. \qquad (24)$$

Then we substitute equation (21) (23) (24) into (22), and obtain the elements of the Hessian matrix

$$\begin{aligned}\frac{\partial^2}{\partial k_{xi}\partial k_{xj}}f &= 8\pi^2\mathrm{Re}\{b_j^* \boldsymbol{a}_j'\boldsymbol{X}\boldsymbol{S}'\boldsymbol{W}\boldsymbol{S}\boldsymbol{X}\boldsymbol{a}_i b_i\},\ i \neq j; \\ \frac{\partial^2}{\partial k_{xi}\partial k_{xj}}f &= 8\pi^2\mathrm{Re}\{b_j^* \boldsymbol{a}_j'\boldsymbol{X}\boldsymbol{S}'\boldsymbol{W}\boldsymbol{S}\boldsymbol{X}\boldsymbol{a}_i b_i\} \\ &\quad + 8\pi^2\mathrm{Re}\{\boldsymbol{e}'\boldsymbol{W}\boldsymbol{S}\boldsymbol{X}\boldsymbol{X}\boldsymbol{a}_i b_i\},\ i = j.\end{aligned}$$

References

[1] R. Deichmann, C. Good, and R. Turner, "RF inhomogeneity compensation in structural brain imaging," *Magn Reson Med*, vol. 47, no. 2, pp. 398–402, 2002.

[2] S. Saekho, F. E. Boada, D. C. Noll, and V. A. Stenger, "Small tip angle three-dimensional tailored radiofrequency slab-select pulse for reduced B_1 inhomogeneity at 3 T," *Magn Reson Med*, vol. 53, pp. 479–84, Feb. 2005.

[3] S. Saekho, C. Yip, D. C. Noll, F. E. Boada, and V. Andrew Stenger, "Fast-k_z three-dimensional tailored radiofrequency pulse for reduced B_1 inhomogeneity," *Magn Reson Med*, vol. 55, pp. 719–24, Apr. 2006.

[4] A. C. Zelinski, L. L. Wald, K. Setsompop, V. K. Goyal, and E. Adalsteinsson, "Sparsity-enforced slice-selective MRI RF excitation pulse design," *IEEE Trans. Med. Imag.*, vol. 27, pp. 1213–29, Sept. 2008.

[5] M. Cloos, N. Boulant, M. Luong, G. Ferrand, E. Giacomini, D. Le Bihan, and A. Amadon, "kT-points: short three-dimensional tailored RF pulses for flip-angle homogenization over an extended volume," *Magn Reson Med*, vol. 67, no. 1, pp. 72–80, 2012.

[6] S. J. Malik, S. Keihaninejad, A. Hammers, and J. V. Hajnal, "Tailored excitation in 3D with spiral nonselective (SPINS) RF pulses," *Magn Reson Med*, vol. 67, no. 5, pp. 1303–15, 2012.

[7] S. Rieseberg, J. Frahm, and J. Finsterbusch, "Two-dimensional spatially-selective RF excitation pulses in echo-planar imaging," *Magn Reson Med*, vol. 47, no. 6, pp. 1186–1193, 2002.

[8] L. Zhao, B. Madore, and L. P. Panych, "Reduced field-of-view MRI with two-dimensional spatially-selective RF excitation and UNFOLD," *Magn Reson Med*, vol. 53, pp. 1118–25, May 2005.

[9] M. Davids, B. Guerin, L. Schad, and L. Wald, "Optimization of fast k-space trajectories for 3D spatially selective parallel excitation," in *Proc. Intl. Soc. Magn. Reson. Med.*, p. 1452, 2014.

[10] J. T. Schneider, R. Kalayciyan, M. Haas, S. R. Herrmann, W. Ruhm, J. Hennig, and P. Ullmann, "Inner-volume imaging in vivo using three-dimensional parallel spatially selective excitation," *Magn Reson Med*, vol. 69, no. 5, pp. 1367–1378, 2013.

[11] S. J. Malik and J. V. Hajnal, "3D-FSE Inner Volume Imaging using 3D selective excitation," in *Proc. Intl. Soc. Magn. Reson. Med.*, p. 0948, 2014.

[12] M. Haas, J. Snyder, S. Buchenau, D. Kokorin, J. T. Schneider, P. Ullmann, J. Hennig, and M. Zaitsev, "Selective excitation of arbitrary three-dimensional targets in vivo using parallel transmit," in *Proc. Intl. Soc. Magn. Reson. Med.*, p. 3476, 2012.

[13] H. Sun, J. A. Fessler, D. Noll, and J.-F. Nielsen, "Steady-state imaging with 3D inner volume excitation," in *Proc. Intl. Soc. Magn. Reson. Med.*, p. 2402, 2015.

[14] C. Yip, J. A. Fessler, and D. C. Noll, "Advanced three-dimensional tailored RF pulse for signal recovery in T_2^*-weighted functional magnetic resonance imaging," *Magn Reson Med*, vol. 56, pp. 1050–9, Nov. 2006.

[15] J.-F. Nielsen, D. Yoon, and D. C. Noll, "Small-tip fast recovery imaging using non-slice-selective tailored tip-up pulses and radiofrequency-spoiling," *Magn Reson Med*, vol. 69, pp. 657 – 666, 2013.

[16] H. Sun, J. A. Fessler, D. Noll, and J.-F. Nielsen, "Strategies for improved 3D small-tip fast recovery (STFR) Imaging," *Magn Reson Med*, vol. 72, no. 2, pp. 389–398, 2014.

[17] H. Sun, J. A. Fessler, D. C. Noll, and J.-F. Nielsen, "Steady-state functional MRI using spoiled small-tip fast recovery imaging," *Magn Reson Med*, vol. 73, no. 2, pp. 536–543, 2015.

[18] S. Williams, H. Sun, J.-F. Nielsen, J. A. Fessler, and D. Noll, "A spectral-spatial pulse for improved signal recovery in the small-tip fast recovery (STFR) sequence," in *Proc. Intl. Soc. Magn. Reson. Med.*, p. 919, 2015.

[19] F. Zhao, J.-F. Nielsen, and D. Noll, "Four dimensional spectral-spatial fat saturation pulse design," *Magnetic Resonance in Medicine*, vol. 72, no. 6, pp. 1637–1647, 2014.

[20] F. Zhao, J.-F. Nielsen, S. Swanson, J. A. Fessler, and D. Noll, "Simultaneous fat saturation and magnetization transfer contrast imaging with steady-state incoherent sequences," *Magn Reson Med*, vol. 74, pp. 739–746, 2015.

[21] C. Yip, J. A. Fessler, and D. C. Noll, "Iterative RF pulse design for multidimensional, small-tip-angle selective excitation," *Magn Reson Med*, vol. 54, pp. 908–17, Oct. 2005.

[22] J. Pauly, D. Nishimura, and A. Macovski, "A k-space analysis of small-tip-angle excitation," *J. Mag. Res.*, vol. 81, pp. 43–56, Jan. 1989.

[23] C. Ma, D. Xu, K. F. King, and Z. P. Liang, "Joint design of spoke trajectories and RF pulses for parallel excitation," *Magn Reson Med*, vol. 65, pp. 973–85, Apr. 2011.

[24] D. Yoon, J. A. Fessler, A. G. Gilbert, and D. C. Noll, "Fast joint design method for parallel excitation RF pulse and gradient waveforms considering off-resonance," *Magn Reson Med*, vol. 68, pp. 278–85, July 2012.

[25] D. Chen, F. Bornemann, M. Vogel, L. Sacolick, G. Kudielka, and Y. Zhu, "Sparse parallel transmit pulse design using orthogonal matching pursuit method," in *Proc. Intl. Soc. Magn. Reson. Med.*, p. 171, 2009.

[26] H. Sun, D. S. Weller, A. Chu, S. Ramani, D. Yoon, J.-F. Nielsen, and J. A. Fessler, "Spoke pulse design in magnetic resonance imaging using greedy minimax algorithm," in *Biomedical Imaging (ISBI), 2013 IEEE 10th International Symposium on*, pp. 696–699, IEEE, 2013.

[27] W. A. Grissom, M.-M. Khalighi, L. I. Sacolick, B. K. Rutt, and M. W. Vogel, "Small-tip-angle spokes pulse design using interleaved greedy and local optimization methods," *Magnetic Resonance in Medicine*, vol. 68, no. 5, pp. 1553–1562, 2012.

[28] C. J. Hardy, P. A. Bottomley, M. O'Donnell, and P. Roemer, "Optimization of two-dimensional spatially selective NMR pulses by simulated annealing," *J. Mag. Res.*, vol. 77, pp. 233–50, Feb. 1988.

[29] Y. S. Levin, L. J. Pisani, D. M. Spielman, and . J. M. Pauly, "Trajectory optimization for variable-density spiral two-dimensional excitation," in *Proc. Intl. Soc. Magn. Reson. Med.*, p. 3012, 2006.

[30] C. Yip, W. A. Grissom, J. A. Fessler, and D. C. Noll, "Joint design of trajectory and RF pulses for parallel excitation," *Magn Reson Med*, vol. 58, pp. 598–604, Sept. 2007.

[31] T. Shao, L. Xia, G. Tao, J. Chi, F. Liu, and S. Crozier, "Advanced three-dimensional tailored RF pulse design in volume selective parallel excitation," *Medical Imaging, IEEE Transactions on*, vol. 31, no. 5, pp. 997–1007, 2012.

[32] J. M. Pauly, B. S. Hu, S. J. Wang, D. G. Nishimura, and A. Macovski, "A three-dimensional spin-echo or inversion pulse," *Magn Reson Med*, vol. 29, pp. 2–6, Jan. 1993.

[33] H. Sun, J. A. Fessler, , D. Noll, and J. F. Nielsen, "Joint design of continuous excitation k-space trajectory and RF pulse for 3D tailored excitation," in *Proc. Intl. Soc. Magn. Reson. Med.*, p. 1438, 2014.

[34] J. A. Fessler, "Image reconstruction toolbox." http://web.eecs.umich.edu/~fessler/code/index.html.

[35] M. Engell-Nørregård and K. Erleben, "A projected back-tracking line-search for constrained interactive inverse kinematics," *Computers & Graphics*, vol. 35, no. 2, pp. 288–298, 2011.

[36] C. Kanzow, N. Yamashita, and M. Fukushima, "Levenberg–Marquardt methods with strong local convergence properties for solving nonlinear equations with convex constraints," *Journal of Computational and Applied Mathematics*, vol. 172, no. 2, pp. 375–397, 2004.

[37] J. Kirk, "Traveling salesman program - genetic algorithm." http://www.mathworks.com/matlabcentral/files/13680/tsp_ga.m.

[38] M. Lustig, S.-J. Kim, and J. M. Pauly, "A fast method for designing time-optimal gradient waveforms for arbitrary-space trajectories," *Medical Imaging, IEEE Transactions on*, vol. 27, no. 6, pp. 866–873, 2008.

[39] S. Vaziri and M. Lustig, "The fastest gradient waveforms for arbitrary and optimized k-space trajectories," in *Biomedical Imaging (ISBI), 2013 IEEE 10th International Symposium on*, pp. 708–711, IEEE, 2013.

[40] J. A. Fessler and B. P. Sutton, "Nonuniform fast Fourier transforms using min-max interpolation," *IEEE Trans. Sig. Proc.*, vol. 51, pp. 560–74, Feb. 2003.

[41] M. Davids, M. Ruttorf, F. Zoellner, and L. Schad, "Fast and robust design of time-optimal k-space trajectories in mri," *Medical Imaging, IEEE Transactions on*, vol. 34, no. 2, pp. 564–577, 2014.

[42] U. Katscher, P. Bornert, C. Leussler, and J. S. van den Brink, "Transmit SENSE," *Magn Reson Med*, vol. 49, pp. 144–50, Jan. 2003.

[43] Y. Zhu, "Parallel excitation with an array of transmit coils," *Magn Reson Med*, vol. 51, pp. 775–84, Apr. 2004.

[44] W. Grissom, C. Yip, Z. Zhang, V. A. Stenger, J. A. Fessler, and D. C. Noll, "Spatial domain method for the design of RF pulses in multi-coil parallel excitation," *Magn Reson Med*, vol. 56, pp. 620–9, Sept. 2006.

[45] H. Sun, *Topics in steady-state MRI sequences and RF Pulse optimization*. PhD thesis, University of Michigan, Ann Arbor, MI, USA, May 2015.

[46] N. O. Addy, H. H. Wu, and D. G. Nishimura, "Simple method for MR gradient system characterization and k-space trajectory estimation," *Magnetic Resonance in Medicine*, vol. 68, no. 1, pp. 120–129, 2012.

Joint design of excitation k-space trajectory and RF pulse for small-tip 3D tailored excitation in MRI

Supplementary material

Hao Sun, Jeffrey A. Fessler, Douglas C. Noll, and Jon-Fredrik Nielsen*

To further evaluate our proposed joint RF pulse and k-space trajectory design method, we added this supplementary material showing an inner-volume excitation simulation with acquired brain B0 field map that has greater B0 inhomogeneity than our phantom results in the paper. Also, we changed the excitation pattern from a cube to a short cylinder with 9 cm diameter and 6 cm thickness, which may be useful for, e.g., stack-of-spirals imaging applications.

Figure 1 shows the simulation result. The extended KT-points pulse itself does not generate the best result among all initial trajectories, but it generates the best final results after optimization. We think the reason is that the extended KT-points method can automatically find a proper maximum k-space extent, so it can generate a final result with proper excitation resolution in all directions. As shown in the main text, optimization always improves the excitation results, reducing the NRMSE by 30 to 40% depending on the initialization method.

---

*Hao Sun and Jeffrey A. Fessler are with the Department of Electrical Engineering and Computer Science, University of Michigan, Ann Arbor, MI 48109 USA. Douglas C. Noll and Jon-Fredrik Nielsen are with the Department of Biomedical Engineering, University of Michigan, Ann Arbor, MI 48109 USA. Emails: {sunhao, fessler, dnoll, jfnielse} @ umich.edu
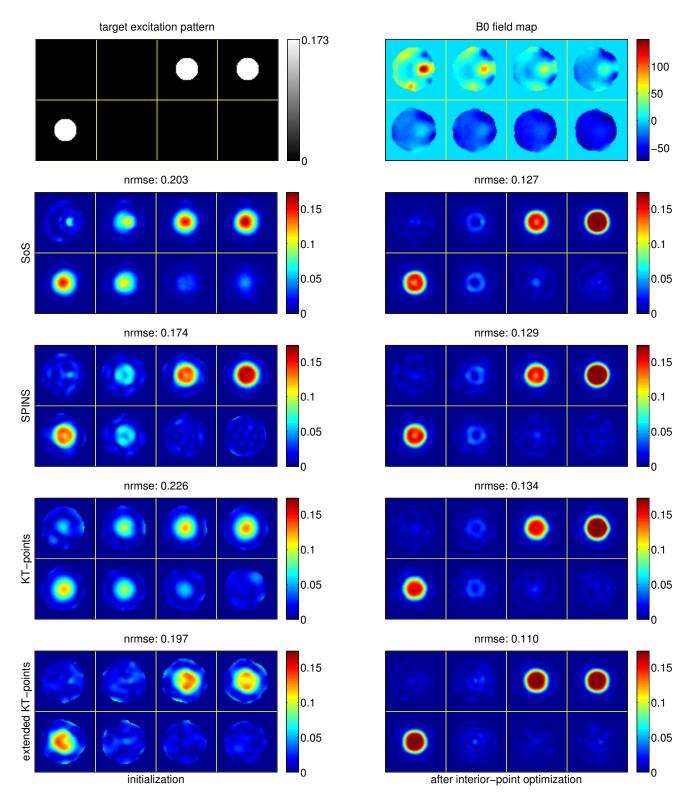
Figure 1: Simulated inner-volume excitation results using a cylinder target pattern (top left) and acquired human brain field map (top right). Rows 2 to 5: result excitation patterns for different pulse design methods: the left column contains the results of the initialization pulse, while the right column contains the results after optimization using the proposed interior point algorithm. Four initialization methods were investigated: SoS, SPINS, KT-points, extended KT-points. All pulses have 3.8 ms pulse length. The extended KT-points pulse generates the best final result after optimization. Optimization always improves the excitation result, reducing the NRMSE by 30 to 40% depending on the initialization method.